Clim. Past Discuss., 8, 6221–6267, 2012
www.clim-past-discuss.net/8/6221/2012/
doi:10.5194/cpd-8-6221-2012

Climate of the Past Discussions

Modelling Northern Hemisphere ice sheets distribution during MIS5 and MIS7 glacial inceptions

F. Colleoni[1], **S. Masina**[1,2], **A. Cherchi**[1,2], **A. Navarra**[1,2], **C. Ritz**[3], **V. Peyaud**[3], and **B. Otto-Bliesner**[4]

[1]Centro Euro-Mediterraneo per i Cambiamenti Climatici, Bologna, Italy
[2]Istituto Nazionale di Geofisica e di Vulcanologia, Bologna, Italy
[3]CNRS/Université Joseph Fourier, Grenoble 1, LGGE, St Martin d'Hères cedex, France
[4]Climate and Global Dynamics Division, National Center for Atmospheric Research, Boulder, CO, USA

Received: 14 November 2012 – Accepted: 5 December 2012 – Published: 18 December 2012

Correspondence to: F. Colleoni (flocolleoni@gmail.com)

Published by Copernicus Publications on behalf of the European Geosciences Union.

Abstract

The present manuscript compares the last two glacial inceptions, Marine Isotope Stage 5 (MIS5, 125–115 kyr BP) and MIS7 (236–229 kyr BP) with the aim to detect the relative impact of external forcing (orbitals and GHG) and ice-albedo feedbacks on the ice sheets growth and distribution in the Northern Hemisphere high latitudes. In order to investigate the differences between those two states, we combine atmosphere-ocean coupled model experiments and off-line ice-sheet-model simulations. In particular, we use a low resolution coupled Atmosphere-Ocean-Sea-ice general circulation model to simulate the mean climate of the four time periods associated with the inception states of MIS5 and MIS7 (i.e. 236, 229, 125 and 115 kyr BP). The four mean states are then use to force a 3-D thermodynamical ice sheet model by means of two types of ice sheet experiments, i.e., steady-state and transient experiments. Our results show that steady-state ice experiments underestimate the ice volume at both 229 kyr BP and 115 kyr BP. On the other hand, the simulated pre-inception ice distributions at 236 kyr BP and 125 kyr BP are in good agreement with observations indicating that during these periods feedbacks associated with external forcing dominate over other processes. However, if proper ice-elevation and albedo feedbacks are not taken into consideration, the evolution towards glacial inception in terms of ice volume and extent is hardly simulated. The experimental setup chosen allows us to conclude that, depending on the mean background climate state, the effect of model biases on climate are more important during a cold inception, such as MIS7, than during a warm inception, such as MIS5. The last results suggest to be cautious when tuning and calibrating Earth System Models on a specific time period, mainly for the purpose of ice sheet-climate coupling.

CPD
8, 6221–6267, 2012

1 Introduction

Glacial inceptions represent a transition from a warm to a cold mean climate state (Calov et al., 2005b). Indeed, considering the sea level record during these warm-to-cold transitions, Northern Hemisphere ice sheets were only little developed over North America and Eurasia compared to glacial maxima (Fig. 1d). Concerns about the capability of climate models to properly simulate future climates have emerged from the large uncertainties and lack of flexibility of the same models to simulate past climate transitions from warm to cold conditions (Calov et al., 2005b). Therefore, glacial inceptions are an interesting phenomenon with which to test the capability of models to simulate climates slightly warmer or slightly colder than present-day climates.

It is now accepted that Northern Hemisphere ice sheets started to develop only if both insolation and greenhouse gases (GHG) dropped significantly (e.g. Berger, 1978; Bonelli et al., 2009). But are all glacial inceptions similar in term of initial continental ice volume? While the maximum sea-level fall was similar between the last two glacial cycles, the maximum sea-level rise during the last two interglacials ($\approx$ 135 kyr BP and $\approx$ 245 kyr BP) varies with estimates above or below present-day sea level (Fig. 1d, Rabineau et al., 2006; Caputo, 2007). Indeed, for the last interglacial ($\approx$ 135 kyr BP), proxies indicate a sea-level rise between 4 to 10 m above mean sea-level (a.m.s.l., Stirling et al., 1995; Kopp et al., 2009; McCulloch and Esat, 2000) implying that part of present-day Antarctica and Greenland ice sheets melted out. In contrast, Dutton et al. (2009) suggest that during the penultimate interglacial, $\approx$ 245 kyr BP, sea-level never rose above present-day mean sea-level. All together, these observations suggest that the amount of continental ice melting differed from one interglacial to another and that the inception of each glacial cycle had different initial conditions at the surface, especially in terms of ice distribution and ice volume stored on the continents. Because of those sea-level characteristics, in this work we focus on the last two glacial inceptions, Marine Isotope Stage 5 (MIS5, $\approx$ 125–116 kyr BP) and MIS7 ($\approx$ 236–229 kyr BP), respectively.

CPD
8, 6221–6267, 2012

Numerous studies have tackled the glacial inception issue using Atmospheric General Circulation Models (AGCM, e.g. Rind et al., 1989; Dong and Valdes, 1995; Vettoretti and Peltier, 2003), coupled Atmosphere-Ocean GCMs (AOGCM, e.g. Khodri et al., 2001; Yoshimori et al., 2002), Earth system Models of Intermediate Complexity (EMIC, e.g. Meissner et al., 2003), and three-dimensional ice sheets models coupled to EMIC (e.g. Calov and Marsiat, 1998; Bonelli et al., 2009). The majority of paleoclimate modelling studies have focused on the last glacial inception (≈ 115 kyr BP) and have simulated a sea-level drop by estimating the amount of perennial snow accumulated over the Northern Hemisphere high latitudes using steady-state experiments (e.g. Vettoretti and Peltier, 2003; Jochum et al., 2012) or transient experiments (e.g. Wang and Mysak, 2002). These models have shown that they can broadly simulate perennial snow and ice sheets growth in the Northern Hemisphere high latitudes where geological evidence are indicative of glacial inception areas. Other studies have performed idealized experiments to determine the thresholds of various regional feedbacks in the climate system that could have triggered a glacial inception in the Northern Hemisphere high latitudes (e.g. Calov et al., 2005a,b). Some of the modeling studies have shown the importance of vegetation and dust in amplifying or inhibiting the growth of the ice sheets during the last two glacial cycles (e.g. de Noblet et al., 1996; Vettoretti and Peltier, 2004; Kageyama et al., 2004; Calov et al., 2005a; Krinner et al., 2006; Colleoni et al., 2009a,b). Kubatzki et al. (2006), using a fully coupled climate-ice-sheet EMIC, showed that during the last glacial inception (≈ 113 kyr BP in their study) the growth of the Laurentide ice sheet could have been delayed by modulating the state of ocean and vegetation. Furthermore, another recent modeling study focusing on the last glacial inception (≈ 115 kyr BP) suggests that the growth of the Eurasian ice sheet at this time was delayed by a persistent high oceanic heat transport towards the Northern Hemisphere high-latitude regions (Born et al., 2010).

Those feedbacks might have not been of similar importance for all the glacial inceptions and therefore it is interesting to determine what were the characteristics of the global climate preceding the inceptions. Recently, Masson-Delmotte et al. (2010)

CPD
8, 6221–6267, 2012

discussed the glacial and interglacial intensities inferred from various climate proxies retrieved from EPICA Dome C, East Antarctica, ice core records. In their work, the last interglacial (≈ 130 kyr BP) appears to be the warmest of the last 800 kyr and was preceded by one of the mildest glacial periods on record, characterized by a moderate sea level drop similar to that occurred at the LGM. In contrast, the penultimate interglacial (≈ 245 kyr BP) was cool and was preceded by one of the coldest glacial periods on record, characterized by a large drop in sea level. In addition, during the last two interglacials, the concentration of atmospheric CO_2 retrieved from East Antarctica (Luthi et al., 2008) peaked to a rather similar value, but dropped by a larger amount during the penultimate glacial inception (Fig. 1f). Indeed, after ≈ 242 kyr BP CO_2 dropped well below 260 ppm, while after 125 kyr BP, CO_2 remained above 260 ppm until ≈ 110 kyr BP. Similarities with GHGs trends are also observed in East Antarctica mean annual temperature anomaly record (Jouzel et al., 2007). In addition the atmospheric CH_4 concentration shows trends similar to CO_2 after both terminations (Fig. 1e, Loulergue et al., 2008). This supports one of the main conclusions of Masson-Delmotte et al. (2010): "cooler" interglacials are preceded by colder glaciations, during which the ice-albedo feedback is particularly large and atmospheric GHGs concentrations are particularly low.

To test the relative importance of orbitals, GHGs and ice-albedo feedbacks on glacial inception processes, we choose to compare the last two glacial inception periods, MIS5 (≈ 125–116 kyr BP) and MIS7 (≈ 236–229 kyr BP) respectively. More specifically we investigate the impact of orbital parameters and GHGs on the growth of ice sheets in the Northern Hemisphere high latitudes. In that context, the last two inceptions are particularly suitable to test the efficiency of the models used here since the MIS5 inception is globally warmer than MIS7. We use an Earth System Model (in its fully AOGCM coupled version) to simulate the climate of those inceptions, and we further use that climate to force a dynamical ice sheet model. In the following sections, the focus is on the ice sheet simulations and the description of the simulated climate dynamics is

CPD
8, 6221–6267, 2012

here restricted to the variables needed by the ice sheet model. Finally the discussion highlights the main weaknesses of the results obtained in this work.

2 Methods

Since the climate model that we use in this work does not have any dynamical ice sheet component coupled to atmosphere and ocean, we force offline a 3-D thermodynamical ice sheet model with our climate simulations. Calov et al. (2009) showed that asynchronous simulations between climate models and ice sheet models in the context of glacial inception are as satisfying as coupled climate-ice sheet simulations. The only difficulty with this method is to account for the evolution in time of the main feedbacks that trigger glacial inception. Therefore, to compensate for this problem, we modulate the climate forcing in our ice sheet experiments by means of a temperature index retrieved from Greenland ice cores. This method has been already used in several studies focusing on particular slices of the last cycle and has provided realistic results of the ice sheet evolution (Peyaud et al., 2007; Charbit et al., 2002).

2.1 Community Earth System Model

To simulate past climates, we use the CESM 1.0, which consists of a fully coupled atmosphere-ocean-sea-ice-land model (Gent et al., 2011). The atmospheric component CAM has 26 vertical levels and an horizontal resolution grid of 96×48 (T31) shared with the land component (CLM). The ocean component (POP, displaced pole located over Greenland) has 60 vertical levels and a nominal 3° horizontal resolution in common with the sea-ice component (CICE). CESM 1.0 provides the possibility of computing dynamical vegetation and dynamical aeolian dust distribution, but we turned off those options and prescribed the pre-industrial vegetation cover and dust distribution over continents in all our experiments since in this work we focus only on the impact of external forcing on the Earth's climate.

CPD
8, 6221–6267, 2012

CESM experiments setup

The two glacial inceptions under investigation have been selected using the values of the proxy records displayed in Fig. 1. The four snapshots referring to the inception periods are identified by the vertical blue boxes. For the last glacial cycle, the timing of inception is commonly defined in literature between 116–113 kyr BP. In this study, we set up the inception simulation with 115 kyr BP orbital and GHG values. Determining the timing of the penultimate inception was harder since, as observed on the sea-level records (Fig. 1d), the penultimate glacial cycle does not exhibit a regular decreasing trend in sea level as for the last glacial cycle. This period is characterized by three sea-level high-stands (even if below present-day sea level), the first one occurring right after Termination III towards ≈ 231 kyr BP, the second one occurring towards ≈ 206 kyr BP and the last one occurring toward ≈ 189 kyr BP (Dutton et al., 2009). Considering the sea level evolution, the penultimate inception occurred after 189 kyr BP. On the other hand, considering GHGs and Antarctica temperature anomaly, the largest peaks occurred right after Termination III, setting the beginning of a new cycle towards 240 kyr BP (Fig. 1e and f). Taking the peak GHGs as reference state for the beginning of the new cycle, we selected the penultimate inception period using the epoch of the nearest orbital state presenting characteristics similar with the inception at 115 kyr BP. The simulation was consequently set up with 229 kyr BP orbitals and GHGs values. As stated in the introduction, the climate evolution before those two glacial inceptions was different (Masson-Delmotte et al., 2010). To account for this difference in our ice sheets simulations we set up two additional simulations with settings that were defined at the time of the highest sea level preceding each glacial inceptions (Fig. 1d): one at 125 kyr BP and one at 236 kyr BP.

In summary, five experiments, different in orbital parameters and atmospheric greenhouse gas concentrations, were carried out to explore the discrepancies between MIS5 and MIS7 glacial inceptions: a present-day run (CTR0k) accounting for present-day GHGs values; a control run set to pre-industrial initial conditions (CTR1850); two MIS5

CPD
8, 6221–6267, 2012

experiments set at 125 kyr BP (K125) and 115 kyr BP (K115) and two MIS7 experiments set at 236 kyr BP (K236) and 229 kyr BP (K229) (see Table 1). The two inceptions experiments, K115 and K229, were branched from K125 and K236 respectively after 400 yr of simulation and were then continued over 700 yr. However, to compare the same model years with the branch experiments, CTR1850, K125 and K236 were also continued to 700 model years. A slight drift still persists in the experiments due to the abyssal circulation (not shown). However, we assume that this drift is small enough to not affect our main conclusions.

2.2 Grenoble Ice Shelf and Land Ice model

Since the CESM 1.0 does not include a fully-coupled ice sheet model, we force the stand-alone GRISLI ice sheet model (Ritz et al., 2001) using the mean climate states computed from our experiments (Table 1). GRISLI is a 3-D-thermodynamical ice sheet – ice stream – ice shelf model, able to simulate both grounded and floating ice. The grounded part uses the shallow ice approximation and the ice shelves are thermo-mecanically coupled to the land-ice part. Ice streams are triggered when the sediment layer is saturated by water. For more details about the physics, the reader may refer to Rommelaere and Ritz (1996) and Ritz et al. (2001).

The experiments have been designed on a regular rectangular grid of 40 km resolution from $\approx 47^{\circ}$ N to the North Pole. Since we focus on glacial inceptions and we do not have any informations about dimensions of the Greenland ice sheet for the periods we are modeling, we start our experiments with the present-day Greenland ice sheet topography adapted from ETOPO2 dataset (NOAA, http://www.ngdc.noaa.gov/mgg/global/etopo2.html). However, the spin-up of the Greenland ice sheet to the time periods considered is simulated through our steady-state experiments (see Sect. 2.2.1). Finally, we assume that the residual glacio-isostatic response from the Last Glacial Maximum (≈ 21 kyr BP) is small enough to consider the present-day topography to be in isostatic equilibrium.

CPD
8, 6221–6267, 2012

To simulate the mass balance of ice sheets, GRISLI uses mean annual and mean summer (JJA) air temperatures and mean annual total precipitations simulated by CESM 1.0. Temperature is corrected for elevation changes using a lapse rate of $5\,^{\circ}\mathrm{C\,km^{-1}}$ for mean annual temperature (Abe-Ouchi et al., 2007; Bonelli et al., 2009) and $4\,^{\circ}\mathrm{C\,km^{-1}}$ for mean summer temperature (Bonelli et al., 2009). Precipitation is corrected assuming that mean annual air temperatures are modulated by an exponential law approximating the saturation water pressure (Charbit et al., 2002). The net accumulation corresponds to a fraction of precipitation turned into snow. The ablation is calculated using the Positive Degree Day method (PDD, Reeh, 1991) for which the melting coefficients have been set to $C_{\mathrm{snow}} = 3\,\mathrm{mm\,^{\circ}C^{-1}\,d^{-1}}$ and $C_{\mathrm{ice}} = 8\,\mathrm{mm\,^{\circ}C^{-1}\,d^{-1}}$. Finally, 60 % of surface melt is able to refreeze.

2.2.1 Ice-sheet experiments setup

Two series of experiments were performed: (1) steady-state and (2) transient experiments. To carry out the steady-state experiments, GRISLI was run for 150 000 model-years both for 236 kyr BP (SS236) and 125 kyr BP (SS125) time periods using K236 and K125 CESM climate forcing and starting from present-day topography. The steady-state ran for 229 kyr BP (SS229) and 115 kyrs BP (SS115) were branched from the last iteration of previous steady-state experiments SS236 and SS125. They were forced using K115 and K125 climates and ran for further 150 000 yr (Table 2).

Given the very similar incoming solar radiation pattern at both inception times 115 kyr BP and 229 kyr BP (Fig. 2a and c), simulating the growth of ice sheets by means of steady state experiments might not highlight the possible differences between those two inceptions. The climate memory of ice sheet is about 5 kyr to 10 kyr and accounting for the climate evolution prior to those two inceptions can lead to a different final ice sheets distribution. We then decided to perform transient experiments spanning 236–229 kyr BP and 125–115 kyr BP where the initial ice topography is that of the steady-states SS236 and SS125 for each period respectively. Since we have available only two simulated climatologies for each inception period, the time evolution

CPD
8, 6221–6267, 2012

of temperature between K236 and K229 and between K125 and K115 is linearly interpolated during the runs in the following way:

$$T_{\mathrm{rec}} = T_{\mathrm{S1}} + \frac{T_{\mathrm{S2}} - T_{\mathrm{S1}}}{\mathrm{d}t} - \lambda(S - S_{0k}) \quad (1)$$

where T_{rec} is the air temperature field adjusted interactively during the experiment and corrected for surface elevation changes (lapse rate λ) between initial surface topography S_{0k} and the new computed surface topography, dt is the intregation time-step of GRISLI (one year), T_{S1} and T_{S2} correspond to the simulated air temperature from climate experiments (Table 1) between which the interpolation is performed during run time.

Since the time evolution of climate between each simulated climatology might not be rigorously linear, the interpolation is adjusted using a temperature index $\Delta T_{\mathrm{index}}$ as follow:

$$T_{\mathrm{rec}} = T_{\mathrm{S1}} + \frac{T_{\mathrm{S2}} - T_{\mathrm{S1}}}{\mathrm{d}t} - \lambda(S - S_{0k}) + \frac{\Delta T_{\mathrm{index}}}{\mathrm{d}t} \quad (2)$$

Similarly, precipitation is interpolated between the two simulated climatologies. However, to account for elevation changes and temperature perturbation, precipitation is adjusted following Charbit et al. (2002):

$$P_{\mathrm{rec}} = (P_{\mathrm{S1}} + \frac{P_{\mathrm{S2}} - P_{\mathrm{S1}}}{\mathrm{d}t}) \cdot e^{[0.05 \cdot (T_{\mathrm{rec}} - T_{\mathrm{S1}})]} \quad (3)$$

where P_{S1} and P_{S2} correspond to simulated CESM precipitation.

2.2.2 Temperature index

Previous studies have realistically simulated the last deglaciation (Charbit et al., 2002), or the Early Weischelian Eurasian ice sheet growth (Peyaud et al., 2007) by means of

CPD
8, 6221–6267, 2012

asynchronous experiments using indices to modulate some of the simulated variables. Transient experiments over the entire last glacial cycle using a coupled climate-ice-sheet model also used indices to modulate some of the simulated variables (aeolian dust deposition in Bonelli et al., 2009, for example.).

To modulate the interpolation of simulated atmospheric temperature, we combined two different published temperature anomaly reconstructions. The first temperature index is the one reconstructed for Greenland over the last two glacial cycles by Quiquet (2012). This index combines three different type of records: North GRIP δ^{18}O record (North GRIP members, 2004), North Atlantic ODP 980 sea surface temperatures record (Oppo et al., 2006) and EPICA Dome C, East Antarctica CH_4 record (Loulergue et al., 2008). The reconstruction is shown in Fig. 3a and the temperature index is expressed as temperature anomaly relative to pre-industrial time period. For more details about the method, see Quiquet (2012).

This temperature index (ΔT_{GR}), based on various types of observations, results from the feedbacks of the entire Earth's climate system. On the contrary, in our climate simulations, we only account for orbitals and GHGs variations. The only simulated ice -Ibedo feedback is due to the sea-ice cover fluctuations. Therefore, the temperature index reconstructed by Quiquet (2012) in its actual shape would not be consistent with our simulations. To retrieve a time evolution temperature index given by the combination of insolation, GHGs and sea-ice albedo, we added the feedbacks calculated by Kohler et al. (2010) by means of an idealized radiative model applied to various proxy records from Antarctica. Indeed, Kohler et al. (2010) managed to calculate the mean annual global temperature anomaly, relative to pre-industrial, resulting from the main climate feedbacks acting at paleo-timescale as:

$$\Delta T^K_{\text{tot}} = \Delta T^K_{\text{orbit}} + \Delta T^K_{\text{GHG}} + \Delta T^K_{\text{land cryo}} + \Delta T^K_{\text{sea ice}} + \Delta T^K_{\text{veg}} + \Delta T^K_{\text{dust}} \quad (4)$$

Kohler et al. (2010) show that ΔT^K_{tot} represents half of the signal from the temperature anomaly retrieved from deuterium excess in East Antarctica (Jouzel et al., 2007). Moreover, the temperature anomaly that they calculated is global, and to apply it to our ice

CPD
8, 6221–6267, 2012

sheet simulations over the Northern Hemisphere, we would need to estimate the time evolution of polar amplification over the high latitudes. Since we do not have any idea of this evolution over the time periods considered here, and since Kohler et al. analysis includes most of the important feedbacks of the climate system, we used all the results from their Fig. 7 and simply calculated the proportion of total signal (ΔT^K_{tot}) represented by the combination of orbitals ($\Delta T^K_{\text{orbit}}$), GHG ($\Delta T^K_{\text{GHG}}$) and sea-ice ($\Delta T^K_{\text{sea ice}}$). We finally multiplied Quiquet (2012) temperature index ΔT_{GR} by this ratio since ΔT_{GR} corresponds to the evolution of Greenland temperature over time and is consequently more representative of the variation in atmospheric temperature over Northern Hemisphere high latitudes:

$$\Delta T_{\text{GIS}} = \Delta T_{\text{GR}} \times \frac{\Delta T^K_{\text{orbit}} + \Delta T^K_{\text{GHG}} + \Delta T^K_{\text{sea ice}}}{\Delta T^K_{\text{tot}}} \quad (5)$$

Since our climate simulations do not account for land-ice elevation and albedo feedbacks, we further added them based on Kohler et al. (2010) and we obtained a second temperature index to test the impact of this feedback during our inception periods:

$$\Delta T_{\text{LIC}} = \Delta T_{\text{GR}} \times \frac{\Delta T^K_{\text{orbit}} + \Delta T^K_{\text{GHG}} + \Delta T^K_{\text{sea ice}} + \Delta T^K_{\text{land cryo}}}{\Delta T^K_{\text{tot}}} \quad (6)$$

The two indices are displayed for both periods in Fig. 3d and e. Two sets of transient experiments were performed (Table 2) based on the two temperature indices, (1) accounting for orbitals, GHGs and sea-ice albedo variations (T115-GIS and T229-GIS) and (2) additionally accounting for land-ice albedo (T115-LIC and T229-LIC).

CPD
8, 6221–6267, 2012

3 Results

3.1 CESM climate simulations

The orbitals for both inceptions are almost similar since perihelion occurred in mid-January for K115 and at the beginning of February for K229 (Table 1). This leads to a similar solar incoming downward radiation pattern over the Northern Hemisphere high latitudes with colder summers and slightly warmer winters with respect to the pre-industrial control run CTR1850 (Fig. 2). In contrast, pre-inception simulations K125 and K236 are different, with perihelion dates in late July and in early October (Table 1). This has consequences on permanent snow cover, which is likely to disappear in K125 due to the strong summer insolation.

Compared to CTR1850, mean summer air temperature (JJA) for K125 is warmer by about 3 °C over the Northern Hemisphere high latitudes, while for all the other periods it remains cooler by at least 2 °C (Fig. 4a to d). It is interesting to note that from K125 to K115 the reduction in mean summer temperature is approximately 4 °C, while from K236 to K229 the reduction is only about 1 °C. The mean annual global cooling due to both inceptions are moderate if compared to CTR8150: of the order of half a degree for the MIS5 inception period and of about 1 °C for the MIS7 inception, respectively (Table 3). The contribution of the Northern Hemisphere (0°–90° N) to this global cooling evolved from 50 % in K125 to 75 % in K115k, while it only evolved by 8 % from K236 to K229. This suggests that during the MIS7 inception, Antarctica and its associated sea-ice cover contributed almost as much as the Northern Hemisphere glacial features to the mean annual global cooling, while this was not the case during MIS5.

In all the experiments, the Northern Hemisphere mean annual precipitation is reduced by more than 20 % with respect to CTR1850 (Fig. 4e to h). This reduction in mean annual precipitation in K115, K229 and K236, is mainly caused by the cooling due to the imposed external forcing (orbitals and GHGs) and is further strengthened by a substantial thickening of the sea-ice cover (of about 2 m) that causes an increase in the local albedo (not shown e.g. Jackson and Broccoli, 2003). The maximum southward

CPD
8, 6221–6267, 2012

extent of the sea-ice cover (SIC) is fairly similar in all the experiments, with the Norwegian Sea permanently ice free (not shown). In K125, the decrease in mean annual precipitation over the entire Northern Hemisphere high latitudes results from the orbital configuration that causes winters to be particularly cold and dry since they occur at aphelion (Fig. 2b). As a consequence, less snow accumulates during the winter, and the little snow that does accumulate melts during the warm summers.

Due to the variations in temperature and precipitation described above, a permanent snow cover develops in all the experiments but its extent varies according to summer temperature or precipitation spatial patterns. In K236 and K115, permanent snow cover is located all along the continental arctic margins, on Svalbard, on the islands of the Barent Sea and Kara Sea and on the Canadian archipelago (Fig. 5b and c). The American Cordilleras are also covered in K115. In contrast, in K125 and K229, the extent of perennial snow is much reduced and is confined exclusively to the eastern part of the Canadian archipelago, Svalbard and the islands of the Barent Sea and Kara Sea (Fig. 5a and d). However, while permanent snow cover in K125 is reduced due to the warm summer temperatures, the limited spatial cover in K229 mainly results from a lack of precipitation over the areas that are covered by perennial snow in K236.

The climatic features described above seem to be realistic given the initial boundary conditions (Table 1). However the low-resolution CESM is affected by some specific biases. The present-day control run CTR0k underestimates temperatures over Northern Eurasia by more than 20 °C in winter and by about 3 °C in summer (Fig. 6a and b). This is due to a weak North Atlantic heat transport towards high latitudes caused by the low spatial resolution (Jochum et al., 2012; Shields et al., 2012). The cold bias over Siberia induces a substantial reduction in precipitation over these regions of at least 90 % during winter and of about 70 % during summer (Fig. 6c and d) if compared to the Global Precipitation Climatology Project precipitation datasets (GPCP, Adler et al., 2003). On the contrary, both temperature and precipitation are overestimated over the Western part of North America.

CPD
8, 6221–6267, 2012

Despite of those biases, the simulated mean annual central Greenland temperature anomaly (relative to CTR1850, blue squares in Fig. 3b and c) is in good agreement with the temperature index of central Greenland accounting for orbital, GHG and SIC albedo feedback (orange curve in Fig. 3b and c). Assuming that the uncertainty on this temperature index is similar to that of our simulated temperatures, this indicates that our two simulations K125 and K115 are able to capture a realistic impact of orbital, GHG and SIC albedo on temperatures in the Northern Hemisphere. It also suggests that the negative precipitation bias associated with the negative temperature anomaly has a minor impact at those times. However, this might not be the case in K236 and K229 which exhibits mean annual temperature anomalies smaller than that of the temperature index. The temperature anomaly is certainly limited by the lack of precipitation inducing a reduction in the snow cover extent in both experiments, which in turn may affect the snow-albedo feedback.

3.2 Ice-sheet experiments results

In this section we use the simulated air temperature and precipitation previously described to force the GRISLI ice sheet model. In the following the ice volume variations will be expressed in sea-level equivalent (SLE, m) calculated as:

$$\mathrm{SLE} = \frac{\rho_\mathrm{I}}{\rho_\mathrm{W}} \times \frac{\mathrm{thk} \times \Delta x \Delta y}{4\pi R^2 \times A_0} \tag{7}$$

where ρ_I is the ice density (917 g cm^{-3}), ρ_W is the seawater density (1018 g cm^{-3}), thk is the simulated ice thickness, Δx and Δy correspond to the horizontal grid increment (40 km), R stands for the radius of the Earth (3671 km) and A_0 corresponds to the present-day surface ratio between oceans and continents (≈ 0.72).

CPD
8, 6221–6267, 2012

3.2.1 Steady-state ice-sheets experiments

The spatial distribution of the steady-state ice distribution for each experiment (Fig. 7), almost matches the permanent snow cover simulated by CESM (Fig. 5). More specifically, the areas where the ice sheets grow in our experiments correspond to a residence snow time of at least 364 days per year. Nevertheless, the ice volume over Eurasia decreases in SS229 because of reduction in precipitation between K236 and K229 (Fig. 7d), which induces a smaller mass balance than in SS236. In SS236, SS229 and SS115, the main common inception areas are covered by ice sheets except in the Cascades mountains range. Over this particular region, the CESM underestimates precipitation (Fig. 6), thus limiting the growth of ice in GRISLI. However, some mismatch persists over Eastern Siberia due to the lack of precipitation in our experiments over this region that inhibits the growth of ice in GRISLI. Furthermore, contrary to what the permanent snow cover indicates in K229, some ice develops over the Barent and Kara Seas in SS229 (Fig. 7d). This can be explained by the fact that K229 is colder than K236 by about 1 °C (Fig. 4c and d) and the mass balance method used by GRISLI considers that air temperature is cold enough to turn precipitation into snow, even if precipitation in K229 is further reduced by about 20 % compared to K236 (Fig. 4g and h).

The total ice volume simulated in the steady-state experiments is in agreement with observations only for SS125 and SS236 (Fig. 8). In SS125, the simulated final ice volume (i.e., removing about 7.1 m SLE for the present-day Greenland ice sheet) amounts to 1.01 m SLE above present-day mean sea level implying that part of present-day Greenland ice sheet melted during our steady-state experiments. This result is induced by the orbital configuration at 125 kyr BP (Fig. 2) causing warmer summers than today in K125 by about 1 °C to 2 °C over Greenland (Fig. 4b). The SLE value is in line with the various relative sea-level reconstructions displayed in Fig. 8a (red dot) and is also in agreement with the recent work by Stone et al. (2012) who estimate the contribution of the Greenland ice sheet during the last interglacial to be in the range 0.6 m–3.5 m

CPD
8, 6221–6267, 2012

SLE . The simulated final ice volume in SS236 is about 10.95 m SLE below present-day mean sea level, which also fits the range of the various sea-level reconstructions [−35; −10] m SLE (Fig. 8b).

On the contrary, neither SS229 nor SS115 simulated final ice volumes match the range of observations. In SS229, the ice volume reaches −6.60 m SLE while observations suggest a sea level of at least −50 m SLE at that time. Similarly, in SS115, the simulated ice volume is −5.23 m SLE and the observations indicate at least −15 m SLE during that period. The discrepancies between our results and the sea-level reconstructions are, on one hand, due to the fact that in our climate simulations the only feedbacks acting at paleo-timescale are orbitals, greenhouse gas and the albedo of the sea-ice cover and, on the other hand, due to the uncertainties of the sea-level reconstructions themselves. Moreover, as explained in the previous section, the CESM shows a significant negative temperature bias in the Northern Hemisphere high latitudes, which further cools the climate at high latitudes and causes a reduction in precipitation. However, it is difficult to assess the impact of such bias on the ice sheet simulations. A systematic correction of our simulated climate fields in order to reduce it would lead to a slightly warmer climate over the high latitudes and it will strengthen the lack of other critical feedbacks (and the most important in our case is probably the ice-elevation-albedo feedback) in our CESM simulations.

Since our climate simulations only account for orbitals, GHGs, and to some extent, to the effect of the sea-ice albedo, how is it possible that SS125 and SS236 match the relative sea-level observations while the laters result from the entire Earth's climate system evolution and feedbacks? For SS125, the reason is linked to the orbital configuration of the period. Indeed, at 125 kyr BP, the summers are particularly warm and the reduced land-ice distribution induces a sea level higher than present-day one. This also implies that the land-ice-albedo feedbacks are not significant compared to the other regional feedbacks and suggests that when we simulate climate at times where sea-level is equals or higher than present-day, the contributions of orbitals and GHGs to atmospheric temperature are enough to get a reasonable continental ice volume that fits

CPD
8, 6221–6267, 2012

with observations. For SS236, when the orbital configuration places the precession at the end of October, the processes are similar. Part of the snow accumulated during the other seasons will melt, but not entirely as in the case for SS125, and the spatial extent of the permanent snow cover will be limited to the region where summer temperature is particularly cold (Figs. 4d and 5c). However, and contrary to SS125, what maintains the air temperature particularly negative in SS236 is the low level of GHGs (Table 1). Observations suggest a sea level of at least −10 m SLE, which implies that the amount of ice accumulated over continents is more or less equivalent to another present-day Greenland ice sheet. However, the already cold climate context minimizes the impact of the land-albedo feedbacks that would more quickly cool the climate over the inception areas. Consequently, and similarly to SS125, the land-ice albedo feedbacks in the high latitudes at this precise time period would not be particularly important compared to the other regional feedbacks.

3.2.2 Transient ice-sheets experiments

The recent work of Kohler et al. (2010) aimed at calculating the individual contribution of the most important feedbacks acting on paleo-timescale to the mean annual global temperature signal: orbitals, GHGs, land-ice, sea-ice, vegetation and aeolian dust. They show that, during interglacials, the land-ice elevation and albedo feedbacks had a minor impact on the mean annual global temperature signal. On the contrary, they point out that the increasing importance of those feedbacks while climate cools until becoming the most important contribution to the mean annual temperature signal approaching the glacial maxima. Similarly, with the steady-state experiments, we have shown that depending on the time period simulated, the lack of some of the regional feedbacks induces large discrepancies between simulated and observed/reconstructed past sea level variations. To further investigate this issue at those time periods, we performed two sets of transient experiments. The temperature evolution between [K236; K229] and [K125; K115] was modulated by two indices constructed after the work Kohler et al. (2010) and Quiquet (2012) (see Sect. 2.2.2). The first one corresponds to the

CPD
8, 6221–6267, 2012

combined impact of orbitals, GHGs and sea-ice albedo feedbacks on air temperature, ΔT_{GIS} (Eq. 5, Fig. 3d and e, orange curve), and is the combination which more closely represents what our climate experiments K236, K229, K125 and K115 account for, i.e., orbitals, GHGs and sea-ice variations. The second one additionally includes the land-ice albedo-elevation feedback, ΔT_{LIC} (Eq. 6, Fig. 3d and e, magenta curve), since we suspect that this feedback is the most important missing contribution in our experiments. Details are reported in the Methods and in Table 2.

The time evolution of both indices ΔT_{GIS} and ΔT_{LIC} for the [125–115] kyr BP exhibits an increase in temperature up to 6° at 122 kyr BP relative to 125 kyr BP value (Fig. 3d) and a decrease of about 7 °C for ΔT_{GIS} and ≈ 12 °C for ΔT_{LIC} starting after 122 kyr BP similarly to the evolution of the Greenland temperature index from Quiquet (2012) (Fig. 3a and b). For the time period [236–229] kyr BP, the temperature indices are always negative and the time evolution is much moderate than for the [125–115] kyr BP time period, reaching at maximum a 4 °C anomaly for the index ΔT_{LIC} relative to 236 kyr BP value (Fig. 3e). For this period, both indices suggest that the role of combined orbitals, GHGs and sea-ice to the total signal is reduced (Fig. 3a and c). The contribution of the land-ice feedbacks remains also limited and adds only 3 °C to the index ΔT_{GIS}, which is half of the maximum contribution to ΔT_{GIS} reached during the [125–115] kyr BP period (Fig. 3d and e).

The time evolution of the ice volume for each transient experiment is displayed in Fig. 8a and b As expected, the ice volume evolution follows the main trends of the temperature indices. For both T115-GIS and T115-LIC, the ice volume first decreases until 121 kyr BP and then increases with decreasing temperature indices (Fig. 8a). For both T229-GIS and T229-LIC, the ice volume increases all along the simulations (temperature index is never above 0 °C). Theoretically, for both experiments T229-GIS and T115-GIS which start from the steady-state runs SS236 and SS125, assuming no bias in the climate forcing and assuming that the temperature index is reasonable, the final state of ice volume should approximately match that of the steady-state experiments SS229 and SS115 (blue dots on Fig. 8a and b). Indeed, the index ΔT_{GIS} is representative of the

CPD
8, 6221–6267, 2012

same feedbacks. This is the case for T115-GIS which broadly matches the final ice volume of SS115 (Fig. 3a). However, this is not the case of T229-GIS, which shows an ice volume larger by about 5 m SLE (Fig. 3b) compared to SS229. We mainly attribute this mismatch in ice volume to the negative bias in precipitation over the Northern Hemisphere high latitudes identified in the climate forcing of the CESM simulations (Fig. 6 and Shields et al., 2012). We remind that the precipitation field is adjusted during the ice simulations according to the changes in temperature due to variations in surface elevation (see Sect. 2.2.1). If the temperature field becomes more negative during the experiment, the precipitation is increased to compensate for the fact that the climate might become dryer during the transient experiment and to allow for ice accumulation in region initially very dry. However, it is also possible that the reconstructed temperature index ΔT_{GIS} overestimates the contribution of the feedbacks included in its calculation since it is base don central Greenland temperature proxies.

The remaining two transient experiments T115-LIC and T229-LIC account for the effect of the land-ice elevation and albedo feedbacks. The simulation is particularly successful in the case of T115-LIC. The time evolution of the ice volume is in line with sea-level reconstructions which show an abrupt decrease after 120 kyr BP (Fig. 8a, magenta dots). For T229-LIC, the matching is good until around 230 kyr BP when the ice volume decrease slows down (Fig. 8b) due to an increase in temperature of about 2 °C in ΔT_{LIC} at this time (Fig. 3e). However, the results obtained using the temperature index ΔT_{LIC} confirm that the land-ice elevation-albedo feedback is critical during inception times, after the interglacial peak. The mismatch between the final ice volume in T229-LIC and the sea-level reconstructions (about 20 m SLE) can be attributed either to the lack of precipitation in the climate forcing which inevitably limits the ice sheet growth, and also to other missing regional feedbacks, as for example vegetation feedback which seems to be the most important after the land-ice-albedo at this time (Kohler et al., 2010).

The spatial distribution of the simulated final ice volume for each of the transient experiment is shown in Fig. 9. For T115-GIS and T229-GIS (Fig. 9a and b), the distribution

CPD
8, 6221–6267, 2012

remains coherent with that obtained with the steady-state experiments SS115 and SS229 (Fig. 7b and d). In T115-GIS, the ice dome over North America and Eurasia is thinner, but the frozen areas over those regions are larger than in SS115. Note that a depression in the ice dome is visible in central Greenland because the Greenland ice sheet completely melts during the transient simulation until almost 121 kyr BP (not shown), and does not recovered its entire volume at the end of the simulation. This happens also in T115-LIC (Fig. 9c). In T229-GIS, the ice distribution is broadly similar to SS229, some ice grows along the coast of the Baffin Bay and the ice sheets are globally thicker than in SS229. In addition, an ice cap develops over the islands of Eastern Siberia continental shelf in both T115-GIS and T229-GIS (Fig. 9a and b). In T115-LIC and T229-LIC, the ice is much thicker over the areas which are ice covered in T115-GIS and T229-GIS (Fig. 9c and d). Furthermore, the extent of the North American and Eurasian ice sheets is larger, even if the ice is thinner in T115-LIC than in T229-LIC. Some ice also develops over the Cascades mountain range in both simulations.

The only unrealistic feature is the ice accumulation over the Bering Strait and the Kamchatka peninsula in both experiments. It has been shown that the existence of an ice sheet large enough over Eurasia could significantly affect the regional circulation by reducing the moisture advection that usually reaches Eastern Siberian topographic highs, therefore stopping some ice cap from developing in this area (Krinner et al., 2011). However, the CESM simulations do not account for changes in topography caused by ice sheets growth and the circulation patterns remain similar in Eastern Siberia for all the simulation regardless of the period. Therefore, since there is no temperature or precipitation effect induced by a deviated circulation in our climate forcing, some ice develops over Eastern Siberia in the transient ice experiments.

Compared to T115-GIS and T115-LIC, it seems that the much larger simulated ice volume in T229-GIS and T229-LIC is due to the impact on air temperature of the particularlly low GHGs values recorded during the penultimate inception (Table 1). The simulated temperature in K236 allows for an initial ice volume in T229-GIS and T229-LIC (spin-up from SS236) much larger than for T115-GIS and T115-LIC. However, even

CPD
8, 6221–6267, 2012

if the amplitude of the temperature index used for the last inception is larger than for the penultimate one, the experiment T115-LIC is probably not long enough to reach a similar ice volume. Indeed, growing a large ice sheet requires favorable temperature and precipitation conditions but, most of all, enough time.

The individual growth of Eurasian and North American ice sheets (excluding Greenland, including the Cascades mountain range) shows that their expansion is well correlated with their thickening in T115-LIC (dashed lines in Fig. 10b and d) but this correlation is weaker in T115-GIS (solid lines). After a first phase during which the ice-covered area and the ice volume decrease, the expansion and the volume of each ice sheet start increasing again from 121 kyr BP until 116 kyr BP. Contrary to the ice-covered area, the ice volume increases until the end of the experiments showing that both ice sheets are not expending anymore, but only thickening. As expected from the total ice volume displayed in Fig. 8a, the growth of both ice sheets is larger in T115-LIC than in T115-GIS and the North American ice sheet is always larger and bigger than the Eurasian one in both experiments (Fig. 10b and d). Contrary to T115-GIS and T115-LIC, in T229-GIS and T229-LIC, the expansion of the ice sheets is not correlated with their thickening (Fig. 10c and e). In the experiments accounting for orbitals, GHGs and sea-ice albedo only, both ice sheets slightly retreat Northward and Westward with respect to the initial covered area at 236 kyr BP, while their ice volume slightly increases. When additionally accounting for land-ice elevation and albedo feedbacks (T229-LIC), after a first phase of rapid expansion until 234 kyr BP, the ice-covered area stabilizes, although the ice volume largely increases until the end of the experiment (Fig. 10c). Since the input air temperature decreases in both experiments due the negative increment by the temperature index, the only limitation to a larger expansion of the ice sheets during this time period seems to be the reduction of precipitation from 236 kyr BP to 229 kyr BP (Fig. 4g and h).

As shown in Fig. 8a and b, the accumulation rate of ice volume better matches the observations and reconstruction when accounting for the land-ice elevation and albedo feedbacks. In T115-GIS and T115-LIC, the expansion rates and the accumulation rates

CPD
8, 6221–6267, 2012

for both ice sheets are directly proportional (Fig. 10a), indicating that the ice sheets expand as fast as they thicken. On the contrary, in T229-GIS and T229-LIC, those rates indicate that the ice sheets thicken more than they expand. In general, in our experiments the addition of the land-ice elevation and albedo feedbacks makes the ice sheets to grow not only bigger and larger but also faster. From those results, we can deduce that during a cold inception, such as 236–229 kyr BP, the probability to grow bigger ice sheets in a faster way is larger than during a warm inception, such as 125–115 kyr BP. A phenomenon identified in climate models may also strengthen this behavior in coupled climate-ice sheets model, namely, the Small Ice-Cap Instability (SICI, North, 1984). This phenomenon occurs when an ice cap is not large enough to resist to particular climate tipping points such as an increase in solar radiation for example, and disappears rapidly. This instability was first identified in simple diffusive climate models that accounted for ice albedo feedback, but was also found in GCMs and linked to the strength of noise forcing (Lee and North, 1995). This phenomenon is clearly model dependent and might affect glacial inceptions in coupled Earth Climate System models.

4 Discussion and conclusions

With two types of ice sheet experiments, steady-state and transient, we wanted to test the impact of external forcing (orbitals and GHGs) on the growth of ice sheets during the last two glacial inceptions. What we have shown in this work is that the steady-state ice distribution at both inception times differs form the transient one. The steady-state experiments, i.e., forced by steady-state simulated climates, underestimate the ice volume at both inceptions times (229 kyr BP and 115 kyr BP), while the pre-inception simulated ice volume (236 kyr BP and 125 kyr BP) is in good agreement with observations. The results show that external forcing are the dominant factors of the Northern Hemisphere high-latitudes climates during interglacials. However, our transient experiments clearly show that without proper ice-elevation and albedo feedbacks,

CPD
8, 6221–6267, 2012

the evolution towards glacial inception in terms of ice volume and extent is hardly simulated. Indeed, even accounting for the ice-albedo feedback, our results are in good agreement with observations only for the last glacial inception period (MIS5), while the simulated ice volume for the penultimate glacial inception period (MIS7) is underestimated. This suggests that the lack of precipitation over the inception areas caused by the CESM negative temperature bias over the Northern Hemisphere high latitudes stops the ice sheets from developing larger and bigger at that time. Our conclusion is that cold biases are more effective during a cold inception, such as during MIS7, than during a warm inception, such as MIS5.

Coupled ice-sheets-climate simulations using fully coupled General Circulation Models spanning an entire glacial cycle are still a challenge constrained by available computational resources. An alternative to transient coupled simulations able to simulate time varying ice distribution is the approach used in this work: simulate climatologies of the main climate tipping points, as glacial maxima and interglacials, and interpolate the climate in between by modulating temperature and/or precipitation by means of a time varying index representative of those quantities. A nice example of this method is the work of Abe-Ouchi et al. (2007) who performed asynchronous simulations between an atmospheric GCM and an ice sheet model to reconstruct the ice volume evolution during the entire last glacial cycle. They used the Positive Degree Day mass balance scheme from Reeh (1991) (as in GRISLI) and parametrized the input atmospheric surface temperature as the sum of the present-day climatology and the temperature anomalies, which are divided into terms due to ice-sheet-albedo feedback, CO_2, insolation feedback and a residual term (Kohler et al., 2010, followed a similar approach). In their dynamical ice-sheet model, accumulation is based on present-day observations which are modulated, through a power law, by the simulated surface temperature anomaly between two time periods. As in Charbit et al. (2002), the fact that this method is based on present-day climatology allows removal of climate model potential biases. As a result, Abe-Ouchi et al. (2007) were able to broadly reproduce a sea-level drop

CPD
8, 6221–6267, 2012

of about 130 m for the LGM (21 kyr BP), using a lapse rate of 5 °C km^{-1}, in agreement with observations.

On the contrary, in our case, we deliberately use the simulated temperature and precipitation to evaluate the capability of CESM with GRISLI to properly simulate different glacial inceptions. Furthermore, the fact that we use both steady-state and transient experiments allows to highlight several important points for both climate modeling and ice modeling. First of all, the steady-states ice experiments are very useful to understand the limits of climate forcing input in terms of temperature and precipitations. In all numerical modeling, a spin-up of the simulated variables is necessary, especially when thermodynamics is active part of the simulated processes. However, in nature, the state of the Earth's system at a given time depends on its evolution. This is particularly important for the components of the system that have long-term memory of climate changes, such as the deep ocean, the ice sheets and ice caps. Our results show that steady-state experiments are efficient when the feedbacks accounted for into the climate simulations are likely to be the dominant feedbacks active during the epoch considered. In the case of our "interglacial" simulations at 125 kyr BP and 236 kyr BP, orbitals, GHGs and the sea-ice albedo feedbacks are enough to simulate a reasonable steady-state ice distribution. On the other hand, our transient experiments show that for the inception simulations at 115 kyr BP and 229 kyr BP, those three feedbacks are not enough to give an ice volume which fits with the observations. The combination of steady-state and transient ice experiments is highly powerful in our case to evidence limits and biases of our climate forcing.

As we showed, our present-day anthropogenic climate simulation (CTR0k) presents strong winter and summer negative temperature anomalies over the Eurasian inception areas causing a reduction in precipitation. If we assume that the cold bias was likely propagated into our past climate simulations, it could have affected the inception process in GRISLI (i) by enhancing the glacial inception due to the cold summer bias, as previously shown in Vettoretti and Peltier (2003), and/or (ii) by resulting in a significant reduction in precipitation over the Eurasian Arctic regions. However, our transient

CPD
8, 6221–6267, 2012

simulations show that those biases do not have the same importance during MIS5 than during MIS7 and that this importance depends on the mean background climate state of the epoch considered. Indeed, in our "warm" glacial inception (MIS5), the high summer temperature at 125 kyr BP inhibits the growth of ice sheets despite of the negative temperature bias in the high latitudes. Because at that time is the impact of precession on high latitude climate that mostly matters. On the other hand, in our "cold" glacial inception (MIS7) the summer temperature is particularly low, due the low level of GHGs, and causes the climate to be particularly dry. In this case, the dryness strengthens the negative precipitation bias by limiting the amount of ice accumulating over the high latitudes.

To improve those results, an alternative approach could be to apply a correction on precipitation and/or temperatures over the regions affected by the biases. Some previous studies using coupled ice sheets-climate models tested the implementation of "patches" for precipitation over the areas of inceptions to counteract the climate model bias (e.g. Bonelli et al., 2009; Ganopolski et al., 2010). However, applying patches over some particular areas greatly limits the validation of the capability of coupled systems to reproduce glacial inceptions where the geological evidence indicate the presence of past ice sheets. It unnaturally forces the response of the climate and ice-sheet models. Moreover, it also limits investigations of whether coupled systems are able to reproduce different spatial ice sheets distributions during older glacial cycles. This solution might be applied only if the aim of the numerical experiments is beyond the scope of validating and calibrating the models to improve the simulation of climate processes.

A last caveat concerns the resolution of the CESM simulations. Compared to Jochum et al. (2012), we simulated the same glacial inception ($\approx$ 115 kyr BP) starting from a colder mean ocean state spin-up (here 125 kyr BP) and with a coarser horizontal resolution (T31). As a result, the simulated perennial snow cover seems to be slightly less extensive at lower resolution, implying that resolution is important for the simulation of polar processes as suggested in the previous work of Vavrus et al. (2011). Simulating the climate at a higher spatial resolution would considerably improve the glacial

CPD
8, 6221–6267, 2012

inception in the climate models, especially over high topographies where numerous GCMs usually fail to calculate correct precipitation patterns (Bonelli et al., 2009). It would also contribute to resolve the melting processes along the margins of the ice sheets, which are critical for the advance and/or retreat of the ice sheets over continental areas laying below a certain latitude (e.g. Colleoni et al., 2009b).

In literature, some of the numerous climate modeling studies focusing on the last glacial inception (see references in Sect. 1) conclude that they succeed in reproducing glacial inception, only by looking at the extent and amount of perennial snow cover on the Northern Hemisphere high latitudes. If we follow a paleo-data approach, nucleation sites for the first ice dynamics are classically the Canadian Archipelago, the Cascades and the Rocky mountains, the Svalbard and the islands in Barents Sea and Kara Sea. Based on this evidence, it becomes difficult to assess whether a climate model can accurately reproduce glacial inceptions without using a dynamical ice sheet model to define the areas where ice dynamics effectively took place in the past. Results in Charbit et al. (2007) show that the spatial distribution of the simulated ice cover is highly model dependent. In some experiments the extent of ice cover matches that of the perennial snow cover of the GCMs, while in others (as in our experiments) it remains limited to some of the Arctic islands. It is tempting to say that ice experiments leading to growth of ice sheet wherever the snow is perennial in GCMs, even in areas in which geological evidence suggests as "ice free", hold a bias inherited from the climate model. However, the persistence of mismatch between the ice cover in the ice sheet model and the perennial snow cover in the GCMs shows the necessity of better understanding the physics and the schemes embedded in our climate and ice-sheet models in order to perform reliable simulations in various climate contexts. However, the limits of the method used in Charbit et al. (2007), Abe-Ouchi et al. (2007), as well as in our present study, is the absence of direct elevation and albedo feedbacks between atmosphere and ice sheets. As we show with our transient experiments, these feedbacks are important for the ice sheets growth and for their effect on the synoptic circulation (e.g. Kageyama et al., 2004; Liakka and Nilsson, 2010; Herrington and Poulsen, 2012).

CPD
8, 6221–6267, 2012

Our results confirm that glacial inceptions are particularly interesting because they represent transient states between warmer to colder climates (Calov et al., 2005b), when the Northern Hemisphere synoptic circulation is not yet too much affected by changes in topography and the amplitude of the temperature anomaly is not as large as during glacial maxima. They constitute an interesting test for the new generation of coupled Earth System Models.

Acknowledgements. We gratefully acknowledge the support of Italian Ministry of Education, University and Research and Ministry for Environment, Land and Sea through the project GEMINA. Many thanks go to Dorotea Iovino for the stimulating discussion and to Narelle van der'Wel for her help on English writing.

References

Abe-Ouchi, A., Segawa, T., and Saito, F.: Climatic Conditions for modelling the Northern Hemisphere ice sheets throughout the ice age cycle, Clim. Past, 3, 423–438, doi:10.5194/cp-3-423-2007, 2007. 6229, 6244, 6247

Adler, R., Huffman, G., Chang, A., Ferraro, R., Xie, P., Janowiak, J., Rudolf, B., Schneider, U., Curtis, S., Bolvin, D., Gruber, A., Susskind, J., and Arkin, P.: The Version 2 Global Precipitation Climatology Project (GPCP) Monthly Precipitation Analysis (1979–Present), J. Hydrometeorol., 4, 1147–1167, 2003. 6234, 6263

Berger, A. L.: Long-term variations of daily insolation and quaternary climatic changes, J. Atmos. Sci., 35, 2362–2367, 1978. 6223

Bintanja, R. and van de Wal, R. S. W.: North American ice-sheet dynamics and the onset of 100,000-year glacial cycles, Nature, 454, 869–872, 2008. 6258

Bintanja, R., van de Wal, R. S. W., and Oerlemans, J.: Modelled atmospheric temperatures and global sea levels over the past million years, Nature, 437, 126–128, 2005. 6265

Bonelli, S., Charbit, S., Kageyama, M., Woillez, M.-N., Ramstein, G., Dumas, C., and Quiquet, A.: Investigating the evolution of major Northern Hemisphere ice sheets during the last glacial-interglacial cycle, Clim. Past, 5, 329–345, doi:10.5194/cp-5-329-2009, 2009. 6223, 6224, 6229, 6231, 6246, 6247

CPD
8, 6221–6267, 2012

Born, A., Kageyama, M., and Nisancioglu, K. H.: Warm Nordic Seas delayed glacial inception in Scandinavia, Clim. Past, 6, 817–826, doi:10.5194/cp-6-817-2010, 2010. 6224
Calov, R. and Marsiat, I.: Simulations of the Northern Hemisphere through the last glacial-interglacial cycle with a vertically integrated and a three-dimensional thermomechanical ice sheet model coupled to a climate model, Ann. Glaciol., 27, 169–176, 1998. 6224
Calov, R., Ganopolsi, A., Petoukhov, V., Claussen, M., Brovkin, V., and Kutbatzki, C.: Transient simulation of the last glacial inception. Part II: sensitivity and feedback analysis, Clim. Dynam., 24, 563–576, 2005a. 6224
Calov, R., Ganopolski, A., Claussen, M., Petoukhov, V., and Greve, R.: Transient simulation of the last glacial inception. Part I: glacial inception as a bifurcation in the climate system, Clim. Dynam., 24, 545–561, 2005b. 6223, 6224, 6248
Calov, R., Ganopolski, A., Kubatzki, C., and Claussen, M.: Mechanisms and time scales of glacial inception simulated with an Earth system model of intermediate complexity, Clim. Past, 5, 245–258, doi:10.5194/cp-5-245-2009, 2009. 6226
Caputo, R.: Sea-level curves: perplexities of an end-user in morphotectonic applications, Global Planet. Change, 57, 417–423, 2007. 6223
Charbit, S., Ritz, C., and Ramstein, G.: Simulations of Northern Hemisphere ice-sheet retreat: sensitivity to physical mechanisms involved during the Last Deglaciation, Quaternary Sci. Rev., 23, 245–263, 2002. 6226, 6229, 6230, 6244
Charbit, S., Ritz, C., Philippon, G., Peyaud, V., and Kageyama, M.: Numerical reconstructions of the Northern Hemisphere ice sheets through the last glacial-interglacial cycle, Clim. Past, 3, 15–37, doi:10.5194/cp-3-15-2007, 2007. 6247
Colleoni, F., Krinner, G., and Jakobsson, M.: Sensitivity of the Late Saalian (140 kyrs BP) and LGM (21 kyrs BP) Eurasian ice sheet surface mass balance to vegetation feedbacks, Geophs. Res. Lett., 36, L08704, doi:10.1029/2009GL037200, 2009a. 6224
Colleoni, F., Krinner, G., Jakobsson, M., Peyaud, V., and Ritz, C.: Influence of regional factors on the surface mass balance of the large Eurasian ice sheet during the peak Saalian (140 kyrs BP), Global Planet. Change, 68, 132–148, 2009b. 6224, 6247
de Noblet, N., Prentice, I. C., Jousseaume, S., Texier, D., Botta, A., and Haxeltine, A.: Possible role of atmosphere-biosphere interactions in triggering the last deglaciation, Geophys. Res. Lett., 23, 3191–3194, 1996. 6224
Dong, B. and Valdes, P.: Sensitivity studies of Northern Hemi- sphere glaciation using an atmospheric general circulation model, J. Climate, 8, 2471–2496, 1995. 6224

CPD
8, 6221–6267, 2012

Dutton, A., Bard, E., Antonioli, F., Esat, T. M., Lambeck, K., and McCulloch, M. T: Phasing and amplitude of sea-level and climate change during the penultimate interglacial, Nat. Geosci., 2, 355–359, 2009. 6223, 6227

Ganopolski, A., Calov, R., and Claussen, M.: Simulation of the last glacial cycle with a coupled climate ice-sheet model of intermediate complexity, Clim. Past, 6, 229–244, doi:10.5194/cp-6-229-2010, 2010. 6246

Gent, P. R., Danabasoglu, G., Donner, L. J., Holland, M. M., Hunke, E. C., Jayne, S. R., Lawrence, D. M., Neale, R. B., Rasch, P. J., Vertenstein, M., Worley, P. H., Yang, Z.-L., and Zhang, M.: The Community Climate System Model Version 4, J. Climate, 24, 4973–4991, 2011. 6226

Herrington, A. R. and Poulsen, C. J.: Terminating the Last Interglacial: The Role of Ice Sheet-Climate Feedbacks in a GCM Asynchronously Coupled to an Ice Sheet Model, J. Climate, 25, 1871–1882, 2012. 6247

Jackson, C. and Broccoli, A.: Orbital forcing of Arctic climate: mechanisms of climate response and implications for continental glaciations, Clim. Dynam., 21, 539–557, 2003. 6233

Jochum, M., Jahn, A., Peacock, S., Bailey, D., Fasullo, J., Kay, J., Levis, S., and Otto-Bliesner, B.: True to Milankovitch: Glacial Inception in the new Community Climate System Model, J. Climate, 25, 2226–2239, doi:10.1175/JCLI-D-11-00044.1, 2012. 6224, 6234, 6246

Jouzel, J., Masson-Delmotte, V., Cattani, O., Dreyfus, G., Falourd, S., Hoffmann, G., Minster, B., Nouet, J., Barnola, J., Chappellaz, J., Fischer, H., Gallet, J., Johnsen, S., Leuenberger, M., Loulergue, L., Luethi, D., Oerter, H., Parrenin, F., Raisbeck, G., Raynaud, D., Schilt, A., Schwander, J., Selmo, E., Souchez, R., Spahni, R., Stauffer, B., Steffensen, J., Stenni, B., Stocker, T., Tison, J., Werner, M., and Wolff, E.: Orbital and Millennial Antarctic Climate Variability over the Past 800,000 Years, Science, 317, 793–797, 2007. 6225, 6231, 6258

Kageyama, M., Charbit, S., Ritz, C., Khodri, M., and Ramstein, G.: Quantifying ice-sheet feedbacks during the last glacial inception, Geophys. Res. Lett., 31, L24203, doi:10.1029/2004GL021339, 2004. 6224, 6247

Kalnay, E., Kanamitsu, M., Kistler, R., Collins, W., Deaven, D., Gandin, L., Iredell, M., Saha, S., White, G., Woollen, J., Zhu, Y., Chelliah, M., Ebisuzaki, W., Higgins, W., Janowiak, J., Mo, K. C., Ropelewski C., Wang, J., Leetmaa, A., Reynolds R., Jenne, R., and Joseph, D.: The NCEP/NCAR 40-year reanalysis project, B. Am. Meteorol. Soc., 77, 437–470, 1996. 6263

CPD
8, 6221–6267, 2012

Khodri, M., Leclainche, Y., Ramstein, G., Braconnot, P., Marti, O., and Cortijo, E.: Simulating the amplification of orbital forcing by ocean feedbacks in the last glaciation, Nature, 410, 570–574, 2001. 6224

Kohler, P., Bintanja, R., Fischer, H., Joos, F., Knutti, R., Lohmann, G., and Masson-Delmotte, V.: What caused Earth's temperature variations during the last 800,000 years? Data-based evidences on radiative forcing and constraints on climate sensitivity, Quaternary Sci. Rev., 29, 129–145, 2010. 6231, 6232, 6238, 6240, 6244, 6256, 6260

Kopp, R. E., Simons, F. J., Mitrovica, J. X., Maloof, A. C., and Oppenheimer, M.: Probabilistic assessment of sea level during the last interglacial stage, Nature, 462, 863–868, 2009. 6223

Krinner, G., Boucher, O., and Balanski, Y.: Ice-free glacial northern Asia due to dust deposition on snow, Clim. Dynam., 27, 773–777, 2006. 6224

Krinner, G., Diekmann, B., Colleoni, F., and Stauch, G.: Global, regional and local scale factors determining glaciation extent in Eastern Siberia over the last 140,000 years, Quaternary Sci. Rev., 30, 821–831, 2011. 6241

Kubatzki, C., Claussen, M., Calov, R., and Ganopolski, A.: Sensitivity of the last glacial inception to initial and surface conditions, Clim. Dynam., 27, 333–344, 2006. 6224

Laskar, J., Robutel, P., Joutel, F., Gastineau, M., Correia, A. C. M., and Levrard, B.: A long-term numerical solution for the insolation quantities of the Earth, Astron. Astrophys., 428, 261–285, 2004. 6258

Lea, D. W., Martin, P. A., Pak, D. K., and Spero, H. J.: Reconstructing a 350 ky history of sealevel using planktonic Mg/Ca and oxygen isotope records from a Cocos Ridge core, Quaternary Sci. Rev., 21, 283–293, 2002. 6265

Lee, W. and North, G.: Small ice cap instability in the presence of fluctuations, Clim. Dynam., 11, 242–246, 1995. 6243

Liakka, J. and Nilsson, J.: The impact of topographically forced stationary waves on local ice-sheet climate, J. Glaciol., 56, 534–544, 2010. 6247

Loulergue, L., Schilt, A., Spahni, R., Masson-Delmotte, V., Blunier, T., Lemieux, B., Barnola, J.-M., Raynaud, D., Stocker, T., and Chappellaz, J.: Orbital and millennial-scale features of atmospheric CH_4 over the past 800,000 years, Nature, 453, 383–386, 2008. 6225, 6231, 6255, 6258

Luthi, D., Floch, M. L., Bereiter, B., Blunier, T., Barnola, J.-M., Siegenthaler, U., Raynaud, D., Jouzel, J., Fischer, H., Kawamura, K., and Stocker, T.: High-resolution carbon dioxide con-

CPD
8, 6221–6267, 2012

centration record 650,000–800,000 years before present, Nature, 453, 379–382, 2008. 6225, 6255, 6258
Martrat, B., Grimalt, J. O., Shackleton, N. J., de Abreu, L., Hutterli, M. A., and Stocker, T. F.: Destabilizations on the Iberian Margin Four Climate Cycles of Recurring Deep and Surface Water, Science, 317, 502–507, 2007. 6258
Masson-Delmotte, V., Stenni, B., Pol, K., Braconnot, P., Cattani, O., Falourd, S., Kageyama, M., Jouzel, J., Landais, A., Minster, B., Krinner, G., Johnsen, S., Röthlisberger, R., Chappellaz, J., Hansen, J., Mikolajewicz, U., and Otto-Bliesner, B.: EPICA Dome C record of glacial and interglacial intensities, Quaternary Sci. Rev., 29, 113–128, 2010. 6224, 6225, 6227
McCulloch, M. T. and Esat, T.: The coral record of last interglacial sea levels and sea surface temperatures, Chem. Geol., 169, 107–129, 2000. 6223
Meissner, K., Weaver, A., Matthews, H., and Cox, P.: The role of land surface dynamics in glacial inception: a study with the UVic Earth system model, Clim. Dynam., 21, 515–537, 2003. 6224
North, G. R.: The small ice cap instability in diffusive climate models, J. Atmos. Sci., 41, 3390–3395, 1984. 6243
North GRIP members: High-resolution record of northern hemisphere climate extending into the last interglacial period, Nature, 431, 147–151, 2004. 6231
Oppo, D. W., McManus, J. F., and Cullen, J. L.: Evolution and demise of the last interglacial warmth in the subpolar North Atlantic, Quaternary Sci. Rev., 25, 3268–3277, 2006. 6231
Peyaud, V., Ritz, C., and Krinner, G.: Modelling the Early Weichselian Eurasian Ice Sheets: role of ice shelves and influence of ice-dammed lakes, Clim. Past, 3, 375–386, doi:10.5194/cp-3-375-2007, 2007. 6226, 6230
Quiquet, A.: Reconstruction de la calotte polaire du Groenland au cours du dernier cycle glaciaire-interglaciaire à partir de l'association de la modélisation numérique 3D et des enregistrements des carottages glaciaires profonds, Ph.D. thesis, Université Grenoble I, LGGE, 2012. 6231, 6232, 6238, 6239, 6260
Rabineau, M., Berne, S., Olivet, J., Aslanian, D., Guillocheau, F., and Joseph, P.: Paleo sea levels reconsidered from direct observation of paleoshore-line position during glacial maxima (for the last 500,000 yr), Earth Pl. Sc. Lett., 252, 119–137, 2006. 6223
Reeh, N.: Parameterization of Melt Rate and Surface Temperature on the Greenland Ice Sheet, Polarforschung, 5913, 113–128, 1991. 6229, 6244

CPD
8, 6221–6267, 2012

Rind, D., Peteet, D., and Kukla, G.: Can Milankovitch orbital variations initiate the growth of ice sheets in a general circulation model?, J. Geophys. Res., 94, 12851–12871, 1989. 6224
Ritz, C., Rommalaere, V., and Dumas, C.: Modeling the evolution of Antarctic ice sheet over the last 420,000 years: Implications for altitude changes in the Vostok region, J. Geophys. Res., 106, 31943–31964, 2001. 6228
Rommelaere, V. and Ritz, C.: A thermomechanical model of ice-shelf flow, Ann. Glaciol., 23, 13–20, 1996. 6228
Schilt, A., Baumgartner, M., Blunier, T., Schwander, J., Spahni, R., Fischer, H., and Stocker, T. F.: Glacial-Interglacial and Millennial Scale Variations in the Atmospheric Nitrous Oxide Concentration during the last 800,000 Years, Quaternary Sci. Rev., 29, 182–192, 2010. 6255
Shackleton, N. J.: The 100,000-Year Ice-Age Cycle Identified and Found to Lag Temperature, Carbon Dioxide, and Orbital Eccentricity, Science, 289, 1897–1902, 2000. 6265
Shields, C. A., Bailey, D. A., Danabasoglu, G., Jochum, M., Kiehl, J. T., Levis, S., and Park, S. The Low-Resolution CCSM4, J. Climate, 25, 3993–4014, 2012. 6234, 6240
Siddall, M., Rohling, E. J., Almogi-Labin, A., Hemleben, Ch., Meischner, D., Schmelzer, I., and Smeed, D. A.: Sea-level fluctuations during the last glacial cycle, Nature, 423, 853–858, 2003. 6258, 6265
Stirling, C. H., Esat, T., McCulloch, M. T., and Lambeck, K.: High-precision U-series dating of corals from Western Australia and implications for the timing and duration of the Last Interglacial., Earth Planet. Sc. Lett., 135, 115–130, 1995. 6223
Stone, E. J., Lunt, D. J., Annan, J. D., and Hargreaves, J. C.: Quantification of the Greenland ice sheet contribution to Last Interglacial sea-level rise, Clim. Past Discuss., 8, 2731–2776, doi:10.5194/cpd-8-2731-2012, 2012. 6236
Vavrus, S., Philippon-Berthier, G., Kutzbach, J. E., and Ruddiman, W. F.: The role of GCM resolution in simulating glacial inception, Holocene, 21, 819–830, 2011. 6246
Vettoretti, G. and Peltier, W. R.: Post-Eemian Glacial Inception. Part I: The Impact of Summer Seasonal Temperature Bias, J. Climate, 16, 889–911, 2003. 6224, 6245
Vettoretti, G. and Peltier, W.: Sensitivity of glacial inception to orbital and greenhouse gas climate forcing, Quaternary Sci. Rev., 23, 499–519, 2004. 6224
Waelbroeck, C., Labeyrie, L., Michel, E., Duplessy, J. C., McManus, J. F., Lambeck, K., Balbon, E., and Labracherie, M.: Sea-level and deep water temperature changes derived from benthic foraminifera isotopic records, Quaternary Sci. Rev., 21, 295–305, 2002. 6258, 6265

CPD
8, 6221–6267, 2012

Wang, Z. and Mysak, L.: Simulation of the last glacial inception and rapid ice sheet growth in the McGill Paleoclimate Model, Geophys. Res. Lett., 29, 2102, doi:10.1029/2002GL015120, 2002. 6224

Yoshimori, M., Reader, M., Weaver, A., and McFarlane, N.: On the causes of glacial inception at 116 ka BP, Clim. Dynam., 18, 383–402, 2002. 6224

CPD

8, 6221–6267, 2012

Table 1. Climate experiments settings. Greenhouse gas concentrations were retrieved from EPICA Dome C, East Antarctica and come from Luthi et al. (2008) for the CO_2, Loulergue et al. (2008) for the CH_4 and Schilt et al. (2010) for the NO_2 records. The orbital parameters for the Pre-industrial control experiment (CTR1850) were set to 1990 while the greenhouse gas were set at their pre-industrial values. For K115 and K229 experiments, the runs were initialized at the 400th model-year of the K125 and K236 experiments respectively.

ID	Epoch (kyrs BP)	Perihelion date	Obliquity (°)	CO_2 (ppm)	CH_4 (ppb)	NO_2 (ppb)	Spin-up	Length (model years)
CTR0K	1990	Jan 4	23.44	367	1760	316	Present-day	400
CTR1850	1990	Jan 4	23.44	284	791	275	Pre-ind	700
K115	115	Jan 14	22.44	262	472	251	K125 branch	300
K125	125	Jul 23	23.86	276	640	263	125k	700
K229	229	Feb 3	22.22	224	493	256	K236 branch	300
K236	236	Oct 2	22.34	241	481	267	236k	700

CPD
8, 6221–6267, 2012

Table 2. Ice sheet experiments settings. The experiments are split into two groups: steady-state and transient. The steady-states SS229 and SS115 have been branch from SS236 and SS125 respectively. For the transient experiments T115-GIS and T229-GIS, the climate evolution between [236 k–229 k] and [125 k–115 k] is perturbed by a temperature index accounting for insolation, greenhouse gas and sea-ice albedo (ΔT_{GIS}) feedbacks from Kohler et al. (2010). For the transient experiments T115-LIC and T229-LIC, the climate evolution between each climate snapshot is perturbed by a temperature index which accounts in addition for land-ice elevation and albedo feedbacks (ΔT_{LIC}) from Kohler et al. (2010).

ID	ΔT_{GIS} (°C)	ΔT_{LIC} (°C)	Climate	Length (kyr)	Spin-up
SS236			K236	0-150	
SS229			K229	150-300	SS236
SS125			K125	0-150	
SS115			K115	150-300	SS125
T229-GIS	X		K236-K229	8	SS236
T115-GIS	X		K125-K115	10	SS125
T229-LIC		X	K236-K229	8	SS236
T115-LIC		X	K125-K115	10	SS125

CPD
8, 6221–6267, 2012

Table 3. Mean annual air temperature anomaly (°C) for each experiment relatively to CTR1850 for global (ΔT_{glob}) and both hemispheres (ΔT_{NH} and ΔT_{SH}). $\Delta T_{NH/glob}$ corresponds to the ratio (%) between Northern Hemisphere and global mean annual air temperature anomaly relative to CTR1850.

ID	ΔT_{glob}	ΔT_{NH}	ΔT_{SH}	$\Delta T_{NH/glob}$
K115	0.45	−0.68	−0.22	75
K125	−0.43	−0.42	−0.43	50
K229	−0.96	−1.228	−0.70	64
K236	−0.87	−0.97	−0.78	56

CPD
8, 6221–6267, 2012

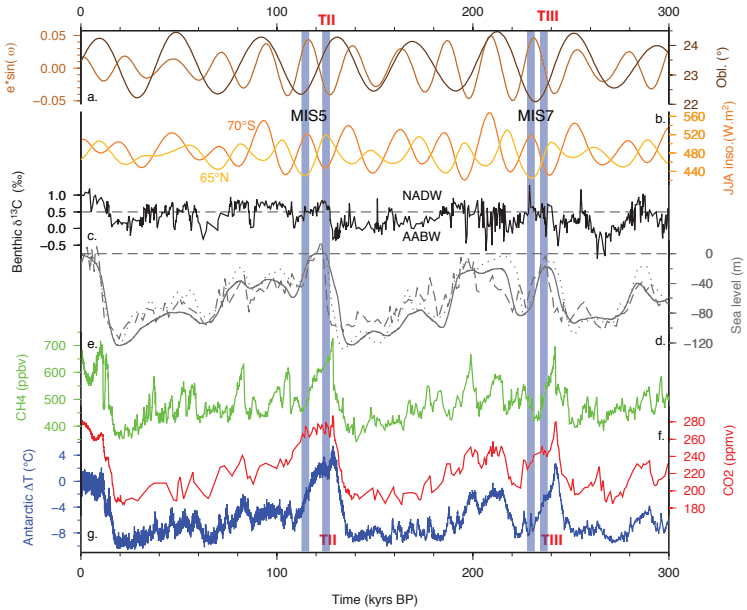

Fig. 1. Overview of the two last glacial cycles illustrated by different forcing and proxies. From top to bottom: **(a)** obliquity (°) and precession index (Laskar et al., 2004); **(b)** summer insolation at 65° N and 70° S (W m^{-2} Laskar et al., 2004); **(c)** benthic δ^{13}C indicative of the changes in sources of the North Atlantic deep waters formation at the Mediterranean latitudes (Martrat et al., 2007); **(d)** sea level reconstructions (m) from Bintaja and van de Wal (2008) (solid line), Siddall et al. (2003) (dashed line) and Waelbroeck et al. (2002) (dotted line); **(e)** atmospheric CH_4 (ppbv) and CO_2 (ppmv) concentrations from EPICA Dome C, East Antarctica (Loulergue et al., 2008; Luthi et al., 2008) and **(f)** EPICA Dome C, East Antarctica, temperature anomaly (°C) relatively to present-day (Jouzel et al., 2007). Vertical grey bars indicate the time of the climate snapshots simulations performed in this work. Termination II (TII) and Termination III (TIII) are indicated as well.

CPD
8, 6221–6267, 2012

Investigating MIS5 and MIS7 glacial inceptions

F. Colleoni et al.

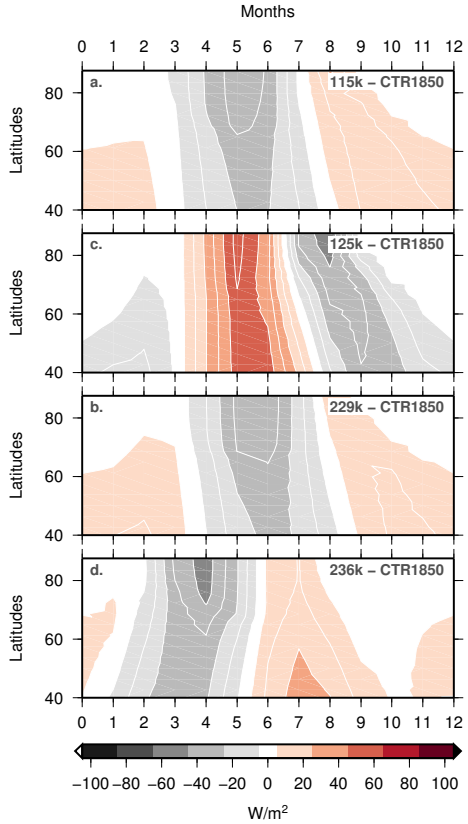

Fig. 2. Solar downward radiation anomaly at top of the atmosphere (W m^{-2}) over the Northern high latitudes (40° N–90° N) between CTR1850 and the experiments described in Table 1.

CPD
8, 6221–6267, 2012

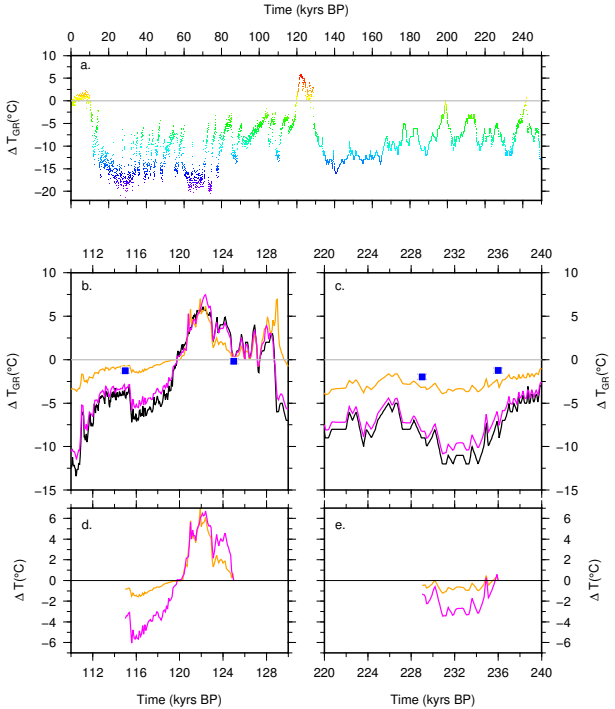

Fig. 3. Temperature indices considered in this work: **(a)** temperature index ΔT_{GR} (anomaly relative to pre-industrial in ˚C) after Quiquet (2012). **(b)** and **(c)** ΔT_{GR} (black) as in **(a)** divided into contribution of combined orbitals, GHGs and sea-ice cover albedo feedbacks (orange) retrived from Kohler et al. (2010) and contribution of additional land-ice albedo feedback (magenta). See Sect. 2.2.2 for more details on the calculations. Blue squares correspond to the simulated mean annual central Greenland temperature anomaly (relative to CTR1850) for each of the CESM experiments (Table 1). **(d)** and **(e)** Temperature indices ΔT_{GIS} and ΔT_{LIC} including orbitals, GHGs and SIC (orange) and additionally accounting for land-ice albedo feedback (magenta) respectively. Temperature anomaly is relative to 125 kyr BP and 236 kyr BP values for each inception period.

CPD
8, 6221–6267, 2012

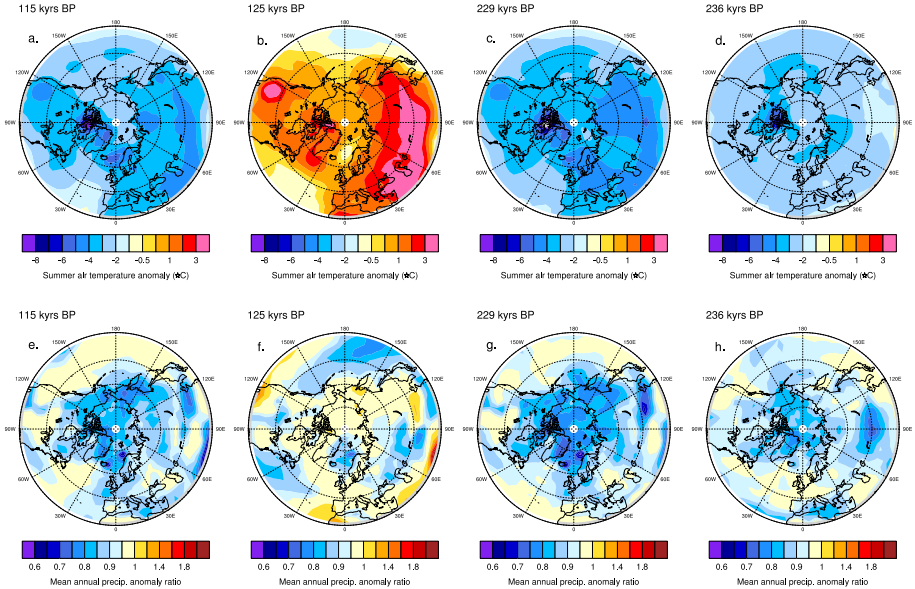

Fig. 4. Simulated air temperatures and precipitation anomalies relatively to pre-industrial control run CTR1850 in the Northern Hemisphere 30° N to 90° N. Top row **(a)** to **(d)**: simulated mean summer air temperature anomaly (June-July-August, JJA) in °C calculated as the difference between each experiment and CTR1850. Bottom row **(e)** to **(h)**: simulated mean annual precipitation anomaly calculated as the ratio between each experiment and CTR1850 (dimensionless).

CPD
8, 6221–6267, 2012

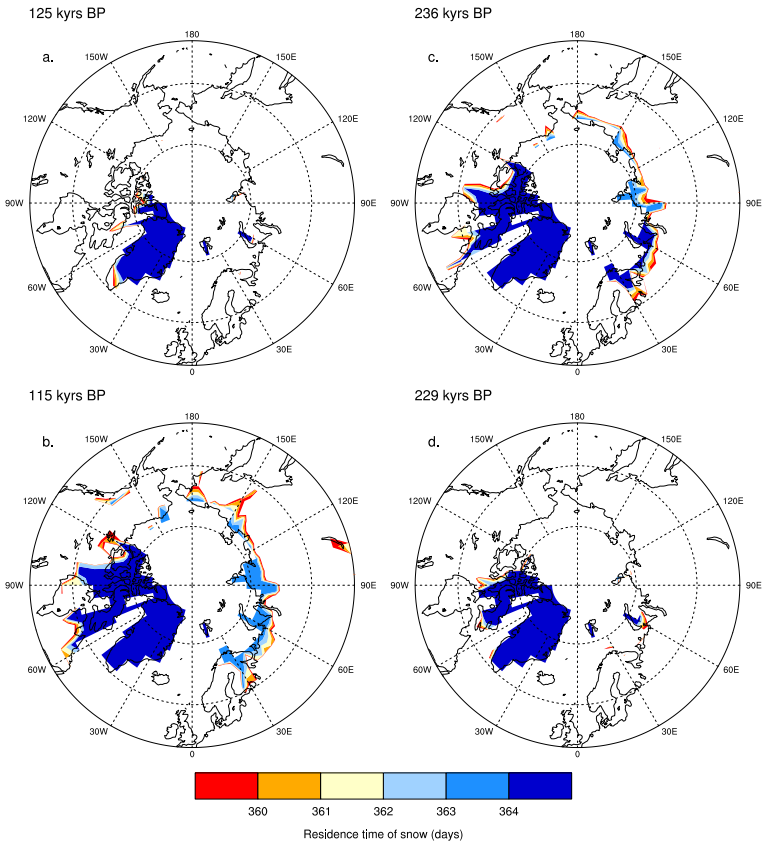

Fig. 5. Simulated residence time (days/year) of snow cover for each climate experiment, **(a)** K125, **(b)**. K115, **(c)** K236 and **(d)** K229. Snow cover is considered permanent when residence time is equal or larger than 365 days (dark blue). Values are shown from 360 days only to increase the legibility of the figure.

CPD
8, 6221–6267, 2012

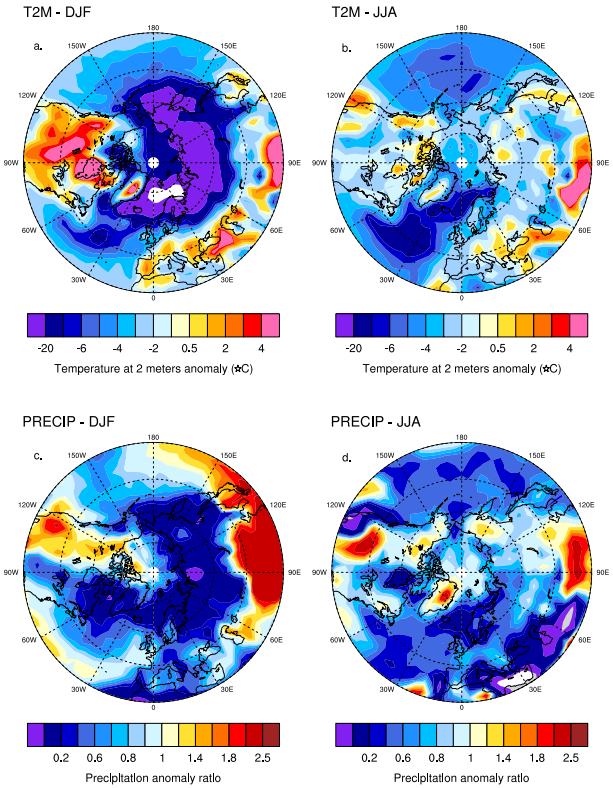

Fig. 6. Bias in temperature an precipitation in the Northern Hemisphere in the low resolution present-day anthropogenic run CTR0k (Table 1) as evidenced by NCEP reanalysis air temperature (Kalnay et al., 1996) and GPCP precipitation dataset (Adler et al., 2003). **(a)** and **(b)** simulated winter (DJF) and summer (JJA) air temperature anomaly (°C) between CTR0k and NCEP reanalysis. **(c)** and **(d)** precipitation anomaly ratio (dimensionless) between CTR0k and GPCP precipitation dataset.

CPD
8, 6221–6267, 2012

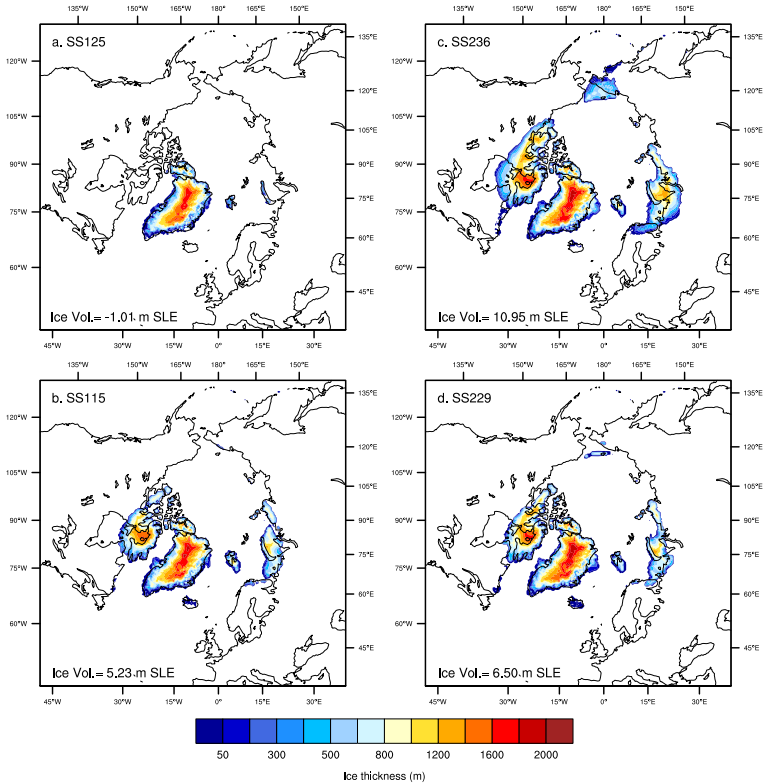

Fig. 7. Simulated ice thickness in meters for each of the steady-state experiment SS125 (**a**), SS115 (**b**), SS236 (**c**) and SS229 (**d**). See Table 2 for details. Simulated total ice volume values for each experiment are expressed in meters Sea Level Equivalent (SLE) and are reported in each frame.

CPD
8, 6221–6267, 2012

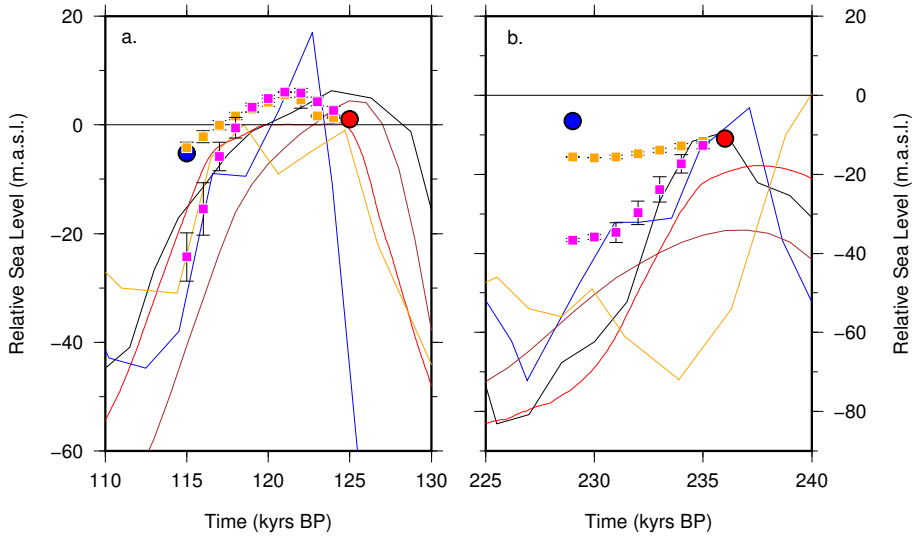

Fig. 8. Ice volume of steady-state experiments (blue and red dots) and of transient experiments (orange and magenta squares) expressed in relative sea-level (m a.s.l.) for MIS5 glacial inception period (**a**) and MIS7 inception period (**b**). Orange squares correspond to transient experiments T115-GIS and T229-GIS ice volume evolution, forced using ΔT_{GIS} index accounting for orbitals, GHGs and SIC. Magenta squares corresponds to T115-LIC and T229-LIC ice volume evolution, forced using ΔT_{LIC} index additionally accounting for land-ice elevation and albedo feedbacks. Simulated values are compared to various sea-level reconstructions: Waelbroeck et al. (2002) (black); Siddall et al. (2003) (blue); Shackleton (2000) (brown); Bintaja et al. (2005) (red) and Lea et al. (2002) (orange).

CPD
8, 6221–6267, 2012

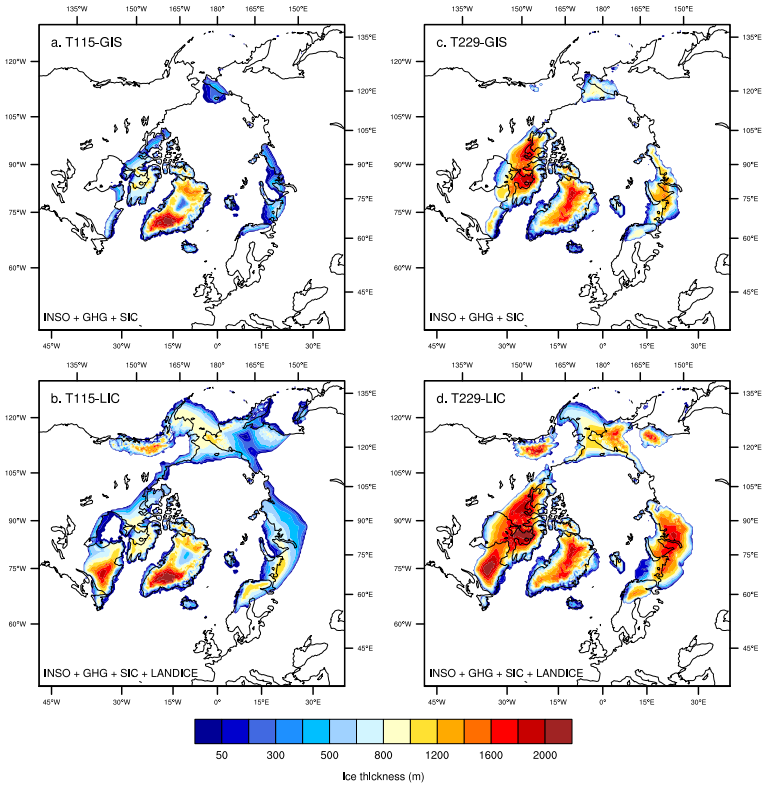

Fig. 9. Simulated ice thickness in meters for each of the transient experiment T115-GIS (**a**), T115-LIC (**b**), T229-GIS (**c**) and T229-LIC (**d**). At the bottom of each frame is indicated the feedbacks included into the temperature indices used to modulate the transient experiments.

CPD
8, 6221–6267, 2012

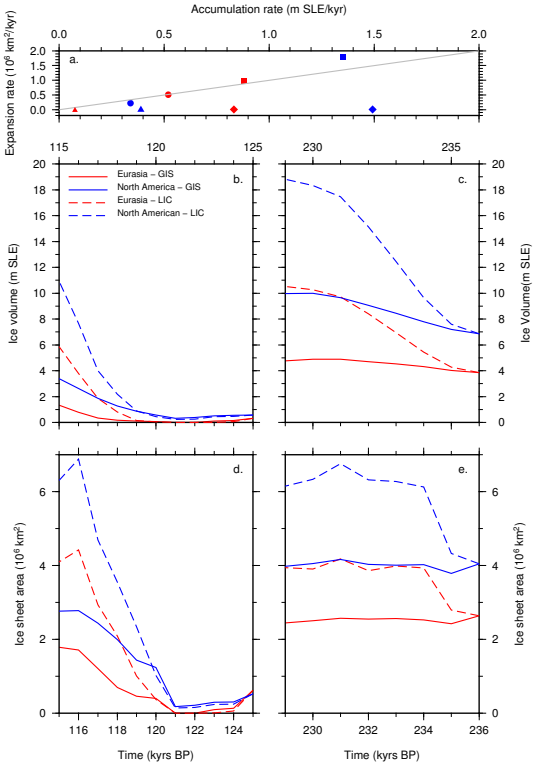

Fig. 10. Simulated time evolution of ice volume (**b** and **c**) and ice-covered areas (**d** and **e**) for each transient experiment T115-GIS, T115-LIC, T229-GIS and T229-LIC, and separated into North American (blue) and Eurasian (red) ice sheets evolution. GIS and LIC refer to temperature indices ΔT_{GIS} and ΔT_{LIC} respectively. Finally, top frame shows the relationship between the expansion rates (10^6 km^2 kyr^{-1}) and the accumulation rates (m SLE kyr^{-1}) of Eurasian (red) and North American (blue) ice sheets for each transient experiments T115-GIS (dots), T115-LIC (squares), T229-GIS (triangles) and T229-LIC (diamonds).

CPD
8, 6221–6267, 2012